Interplay of magnetic field and trigonal distortion in the honeycomb Γ model: Occurrence of a spin-flop phase

Qiang Luo [1,2] and Hae-Young Kee [1,3,*]

[1]*Department of Physics, University of Toronto, Toronto, Ontario M5S 1A7, Canada*
[2]*College of Physics, Nanjing University of Aeronautics and Astronautics, Nanjing 211106, China*
[3]*Canadian Institute for Advanced Research, Toronto, Ontario M5G 1Z8, Canada*

In candidate Kitaev materials, the off-diagonal Γ and Γ′ interactions are identified to come from the spin-orbit coupling and trigonal distortion, respectively. They have generated intense research efforts because of their intimate relation to the field-induced magnetically disordered state reported in α-RuCl$_3$. Theoretically, while a plethora of field-induced phases has been proposed in the honeycomb lattice, a stable intermediate phase that can survive in a wide parameter region regardless of the underlying phases is still lacking. Here we focus on the interplay of an out-of-plane magnetic field and a symmetry-allowed Γ′ term due to trigonal distortion in the dominant antiferromagnetic Γ region. By using multifaceted approaches ranging from classical Monte Carlo and semiclassical spin-wave theory to density-matrix renormalization group, we identify an intriguing spin-flop phase in the presence of magnetic field and antiferromagnetic Γ′ interaction, before it eventually enters into a fully polarized state. As the Γ′ interaction approaches the size of Γ one, the Γ-Γ′ model maps to the easy-axis XXZ antiferromagnet, where the spin-flop phase can be understood as a superfluid phase in the extended Bose-Hubbard model. Our finding thus demonstrates an exciting path from the honeycomb Γ model towards a $U(1)$-symmetric XXZ antiferromagnet in a magnetic field.

I. INTRODUCTION

In the pursuit of exotic quantum ground states such as quantum spin liquid (QSL), a large family of spin-orbit coupled effective spin-1/2 Mott insulators on a honeycomb lattice has been the focus of massive research efforts (for reviews, see Refs. [1,2]). This interest is triggered by a seminal work by Kitaev, who proposed an exactly solvable honeycomb model consisting of bond-directional Ising couplings, and demonstrated that it hosts QSLs with fractionalized excitations of itinerant Majorana fermions and $\mathbb{Z}_2$ gauge fluxes [3]. Jackeli and Khaliullin subsequently showed that the Kitaev (K) interaction could be realized in alkali iridates [4]. However, almost all existing Kitaev materials are found to exhibit long-range magnetic orderings at ambient pressure and zero magnetic field. For example, the well-studied Na$_2$IrO$_3$ [5,6] and α-RuCl$_3$ [7–9] have the zigzag magnetic order at low temperatures, while the Li$_2$IrO$_3$ family displays an incommensurate counterrotating magnetic spiral [10–12]. A newly synthesized compound YbCl$_3$ with $4f$ electron configuration, which is proposed as a possible realization of the Kitaev interaction, shows an antiferromagnetic (AFM) order with a Néel temperature $T_N = 0.60$ K [13–16]. The existence of long-range magnetic orders in these compounds is naturally understood as a consequence of non-Kitaev interactions, which contaminate the fragile Kitaev QSL. The non-Kitaev interactions include the Heisenberg (J) interaction, and also the symmetric off-diagonal Γ and Γ′ interactions, which mainly come from the spin-orbit coupling [17], and trigonal distortion [18], respectively.

Hitherto, α-RuCl$_3$ has drawn immense attention for the existence of fingerprints of fractionalized excitations [19–21]. Also of note is that an in-plane magnetic field of roughly 8 T can suppress the underlying magnetic order, leading to an intermediate phase (IP), which could survive in a finite interval of magnetic field [22–27]. However, the precise nature of this IP is still a contentious question, with a possibility of either Majorana fermionic excitations or conventional multiparticle magnetic excitations [28,29]. Noteworthily, the former scenario is in line with the tempting observation of a half-integer quantized thermal Hall effect [30]. In addition, a convictive model, which harbors such an IP on top of the zigzag ordering is still absent, although there is a consensus regarding the minimal K-Γ model [31,32]. On the other hand, when an out-of-plane magnetic field is applied, a metamagnetic transition due to the possible spin-flop process is also reported but with a large critical magnetic field [33]. The fact that the discrepancy between the in-plane and out-of-plane Landé g factors is modest implies a significant role played by the symmetric off-diagonal Γ interaction. Meanwhile, a small Γ′ interaction stemming from the inevitable trigonal distortion should also be involved [18]. This term is essential for explaining the zigzag ordering in α-RuCl$_3$ [34,35], and could enhance the mass gap of Majorana fermions generated by external magnetic fields [36,37]. Until now, many theoretical models such as J-K model [38], K-Γ-Γ′ model [39,40], and K-Γ-J_3 model [41], have been adopted to embrace the field-induced
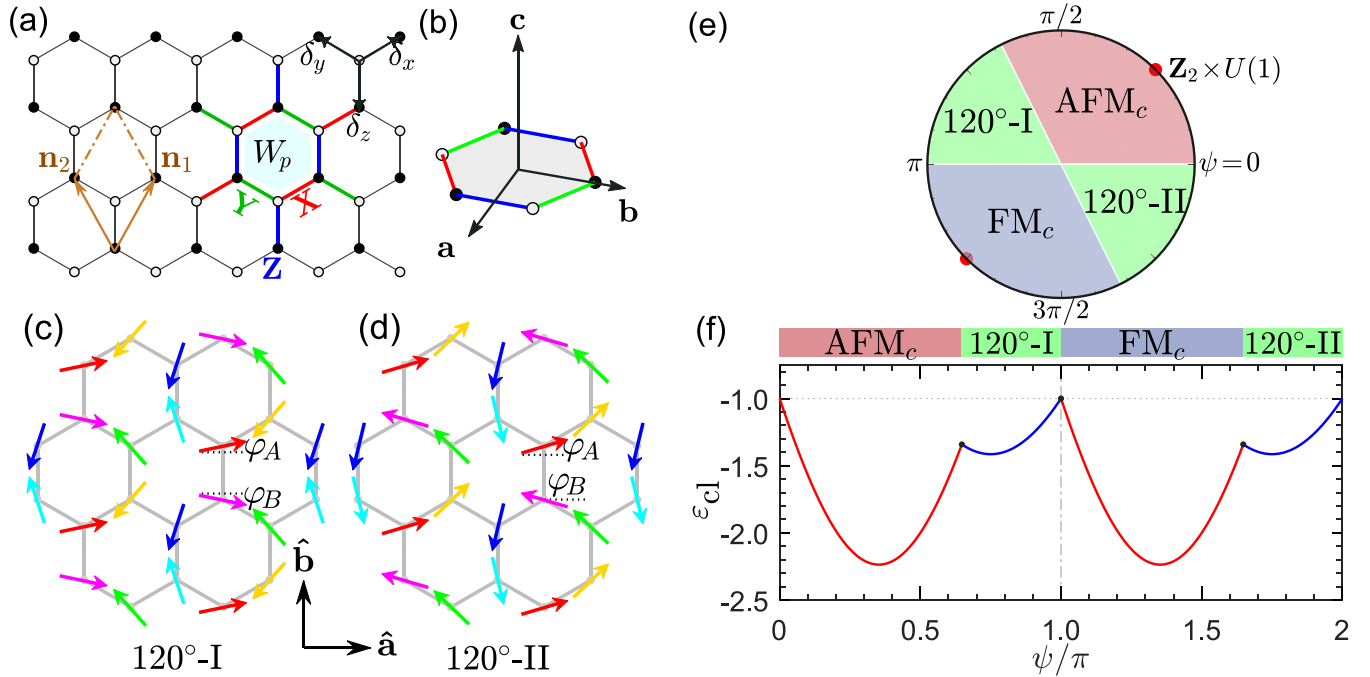
*hykee@physics.utoronto.ca

FIG. 1. (a) Honeycomb lattice with a YC structure. The unit cell defined by primitive vectors $\mathbf{n}_{1,2} = (\pm\sqrt{3}/2, 3/2)$ contains two (open and filled) sites. $\boldsymbol{\delta}_x$ ($\sqrt{3}/2, 1/2$), $\boldsymbol{\delta}_y$ ($-\sqrt{3}/2, 1/2$), and $\boldsymbol{\delta}_z$ ($0, -1$) are the unit vectors along the **X** (red), **Y** (green), **Z** (blue) bonds, respectively. (b) Layout of the honeycomb plane spanned by **a** $[11\bar{2}]$ and **b** $[\bar{1}10]$. **c** [111] represents the out-of-plane direction, which is perpendicular to the honeycomb plane. (c) and (d) show the in-plane spin structures of the 120°-I and 120°-II phases, respectively. Here, φ_A and φ_B are the referring angles of A and B sublattices with respect to the **a** direction. They satisfy the relation $\varphi_A + \varphi_B = 0$ (or 2π) for 120°-I phase and $\varphi_A + \varphi_B = \pi$ (or 3π) for 120°-II phase. (e) Classical phase diagram of the Γ-Γ' model with $\Gamma = \cos\psi$ and $\Gamma' = \sin\psi$, which includes the AFM$_c$ phase, the FM$_c$ phase, and the 120° phases. (f) The classical ground-state energy $\varepsilon_{\mathrm{cl}}$ versus ψ.

IPs that may relate to the experimental phenomena observed in α-RuCl$_3$.

To study the intriguing IPs in the presence of a magnetic field, we start from a Γ-Γ' model with a dominant AFM Γ interaction. Here, the ground state is known to host two exotic phases dubbed Γ spin liquid (ΓSL, named after the ground state of the honeycomb Γ model [42–44]) and chiral-spin ordering stabilized by a small AFM Γ' interaction [45]. The model is equivalent to a $U(1)$-symmetric XXZ model when $\Gamma' = \Gamma$, and the ground state turns out to be an AFM$_c$ state whose magnetic moment is along the **c** [111] direction. A natural question in mind is whether an IP could appear over the disordered phases or AFM$_c$ states in the presence of an external magnetic field. We recall that the uniaxial Heisenberg antiferromagnet undergoes a spin-flop transition when a magnetic field is applied parallel to the easy-axis direction [46,47]. In the spin-flop region, the spins exhibit considerable components that are normal to the field direction, albeit with somewhat canting toward the applied field [48]. To this end, we apply a [111] magnetic field in the Γ-Γ' model, and a spin-flop phase is found to set in above the ΓSL, the chiral-spin ordering, and the AFM$_c$ phase, before entering into the paramagnetic phase at large field. Notably, the spin-flop phase in the parameter region with $\Gamma' = \Gamma$ could be interpreted as a superfluid phase in the hard-core extended Bose-Hubbard model [49,50].

The rest of the paper is organized as follows. In Sec. II, we introduce the generic $JK\Gamma\Gamma'$ model on the honeycomb lattice, followed by a brief mention of our numerical and theoretical methods. In Sec. III, we perform both classical and semiclassical studies of the zero-field Γ-Γ' model, in connection to a previous quantum study [45]. Section IV presents a field-induced quantum phase diagram, with an emphasis on the ΓSL and chiral spin state. In Sec. V, a thorough analysis of the field-induced spin-flop phase is shown. Finally, conclusions are presented in Sec. VI.

II. MODEL AND METHODS

In the multitudinous Kitaev materials with spin-orbit coupled pseudospin-1/2 degrees of freedom, the paradigmatic model takes the general $JK\Gamma\Gamma'$ form on a honeycomb lattice [17,18],

$$
\begin{aligned}
\mathcal{H} = \sum_{\langle ij \rangle \| \gamma} & \left[J\mathbf{S}_i \cdot \mathbf{S}_j + KS_i^\gamma S_j^\gamma + \Gamma\left(S_i^\alpha S_j^\beta + S_i^\beta S_j^\alpha\right) \right] \\
& + \Gamma' \sum_{\langle ij \rangle \| \gamma} \left[\left(S_i^\alpha + S_i^\beta\right)S_j^\gamma + S_i^\gamma\left(S_j^\alpha + S_j^\beta\right) \right] \\
& - \sum_i \widehat{\mathbf{h}} \cdot \mathbf{S}_i,
\end{aligned}
\tag{1}
$$

where S_i^γ ($\gamma = x$, y, and z) is the γ component of spin-1/2 operator at site i. On z bonds $(\alpha, \beta, \gamma) = (x, y, z)$, with cyclic permutation for x and y bonds [see Fig. 1(a)]. J and K are the diagonal Heisenberg and Kitaev interactions, respectively, while Γ and Γ' are the symmetry-allowed off-diagonal exchanges. The last term in Eq. (1) specifies a uniform external

magnetic field $h = |\hat{\mathbf{h}}|$ in the [111] direction, which is perpendicular to the honeycomb lattice as illustrated in Fig. 1(b). On account of the possible microscopic Hamiltonian of α-RuCl$_3$, the model (1) has been studied previously with K, Γ being treated as leading interactions [39,40,51]. From a theoretical point of view, the AFM Kitaev model in a [111] magnetic field has been studied extensively and a QSL is found in an intermediate field despite that its nature is still under study (see Ref. [52] and references therein). On the other hand, near the dominant AFM Γ region, the ΓSL and the chiral spin phase are identified by tuning the Γ' term [45].

In the subsequent sections, we will perform a hierarchical study of the Γ-Γ' model in a [111] magnetic field where the Heisenberg (J) interaction and the Kitaev (K) interaction are switched off. The classical Luttinger-Tisza method is used to map out the zero-field phase diagram [53,54], while the classical Monte Carlo (MC) simulation is performed in the presence of a finite magnetic field [55]. The simulations are executed in a low-temperature range with dozens of replicas. For each given temperature, we use the heat-bath algorithm to target the lowest energy with a MC step of 5×10^6. In addition, the thermal replicas where configurations swap between different temperatures are allowed with a probability according to a detailed balance condition [56]. When considering the effect of quantum fluctuations, we calculate the spin-wave energy, dispersion relations, and the Chern number with the help of linear spin-wave theory (LSWT) [57].

Apart from the classical and semiclassical treatments, this model is studied massively by the density-matrix renormalization group (DMRG) method on two distinct cluster geometries [58–60]. The DMRG is initially invented as a powerful approach aiming to solve problems in one dimension, and stands out as a competitive method for dealing with two-dimensional problems. In the latter case, one needs to map the physical two-dimensional lattice to the one-dimensional chain properly. This process will inevitably involve long-range correlation and entanglement [60]. However, these issues are not very severe if the number of sites is not too large or the width of the cylinder is not too big, and could be reduced essentially by increasing the block states and performing finite-size scaling. We focus primarily on a 24-site C_6-symmetric hexagonal cluster under full periodic boundary condition, and the method to map it to a one-dimensional chain is shown in the Supplemental Material [61]. In addition, we also consider the $L_x \times L_y$ YC cluster under cylindrical boundary condition with total sites $N = L_x L_y$ [cf. Fig. 1(a)]. During the calculation, the truncation error will change as we scan the superblock and it also decreases with the increase of the block state. Therefore, we keep as many as $m = 3000$ block states and perform up to 12 sweeps until the worst truncation error is smaller than 10^{-6}.

III. CLASSICAL AND SEMICLASSICAL STUDY OF THE Γ-Γ' MODEL

A. Lutinger-Tisza analysis

Before presenting the quantum study of the Γ-Γ' model, it is helpful to have a look at the classical phase diagram. The Luttinger-Tisza method has been demonstrated to be powerful

for the determination of magnetic ground states in various classical spin models [53,54]. In these models, the classical spins are treated as $O(3)$ vectors, which satisfy the condition $|\mathbf{S}_i|^2 = S^2$. In the spirit of the Luttinger-Tisza method, this hard constraint is replaced by a soft constraint $\sum_i |\mathbf{S}_i|^2 = NS^2$ tentatively, and the authentic ground state is selected from those solutions derived under the soft constraint that additionally meets the hard constraint. Successful applications of the Luttinger-Tisza method to the spin-orbit coupled model (1) in some special cases are shown previously [62,63].

We choose the primitive vectors of the honeycomb lattice as $\mathbf{n}_{1,2} = (\pm\sqrt{3}/2, 3/2)$ [see Fig. 1(a)], and the sites are represented as $(\mathbf{R}, \upsilon)$, where $\mathbf{R}$ marks the position of the unit cell and υ (= 1, 2) is the sublattice index. Transforming the spin operators via $\vec{S}_{\mathbf{R},\upsilon} = \sum_q e^{iq\cdot\mathbf{R}} \vec{S}_{q,\upsilon}$ with $\vec{S}_{q,\upsilon} = (S^x_{q,\upsilon}, S^y_{q,\upsilon}, S^z_{q,\upsilon})^T$, we cast the entire Hamiltonian in the reciprocal space as

$$\mathcal{H}/N = \frac{1}{4} \sum_q \left(\vec{S}^T_{-q,1}, \vec{S}^T_{-q,2}\right) \cdot \mathbf{\Lambda}_q \cdot \begin{pmatrix} \vec{S}_{q,1} \\ \vec{S}_{q,2} \end{pmatrix}, \qquad (2)$$

where the 6×6 interaction matrix $\mathbf{\Lambda}_q$ is an antidiagonal block matrix

$$\mathbf{\Lambda}_q = \begin{pmatrix} \vec{0} & \mathbf{\Delta}_q \\ \mathbf{\Delta}_q^* & \vec{0} \end{pmatrix}.$$

Here,

$$\mathbf{\Delta}_q = \begin{pmatrix} \mathcal{K}(\varsigma_1) & \mathcal{T}(1) & \mathcal{T}(\varsigma_2) \\ \mathcal{T}(1) & \mathcal{K}(\varsigma_2) & \mathcal{T}(\varsigma_1) \\ \mathcal{T}(\varsigma_2) & \mathcal{T}(\varsigma_1) & \mathcal{K}(1) \end{pmatrix},$$

with $\mathcal{K}(\varsigma) = J\gamma_k + \varsigma K$ and $\mathcal{T}(\varsigma) = \Gamma'\gamma_k + \varsigma(\Gamma - \Gamma')$. The momentum-dependent arguments read as

$$\varsigma_{1,2} = e^{-\iota q \mathbf{n}_{1,2}} = e^{-\iota(\pm\sqrt{3}q_x + 3q_y)/2}$$

and

$$\gamma_q = 1 + \varsigma_1 + \varsigma_2 = 1 + 2\cos\frac{\sqrt{3}q_x}{2} e^{-\iota 3q_y/2}.$$

According to the Luttinger-Tisza minimization, the lowest eigenvalue of $\mathbf{\Lambda}_q$ in the entire Brillouin zone provides a lower bound of the classical energy. Noticing that $\mathcal{D}_q = \mathbf{\Delta}_q^* \mathbf{\Delta}_q = \mathbf{\Delta}_q^\dagger \mathbf{\Delta}_q$, we find that

$$E/(NS^2) \geqslant -\frac{\sqrt{\lambda_{\max}}}{2}, \qquad (3)$$

where $\lambda_{\max}$ is the maximal eigenvalue of $\mathcal{D}_q$ at the corresponding ordering wave vector $\mathbf{Q}$. The magnetic moment direction $\vec{m}$ can be obtained afterwards by checking the spin-length constraint.

We have applied the Luttinger-Tisza method to the Γ-Γ' model, and the corresponding classical phase diagram is found to include an AFM$_c$ phase when $\Gamma' > 0$ and a ferromagnetic (FM$_c$) phase when $\Gamma' < 0$. Here, the subscript c represents that magnetic moment direction is along the **c** [111] direction. The energy of the AFM$_c$ phase is $\varepsilon_{\text{cl}} = -(\Gamma + 2\Gamma')$, while it is $\Gamma + 2\Gamma'$ for FM$_c$ phase. The classical phase diagram also contains two 120° phases but with different relative angles [see Figs. 1(c) and 1(d)]. For the 120° phases, all spins lie

in the ab plane and are divided into two interpenetrating parts on A and B sublattices of honeycomb lattice, where on each sublattice the spins on the corner of an equilateral triangle are mutually oriented to each other with 120 angles. Assuming that φ_A and φ_B are the in-plane angles of A and B sublattices with respect to the **a** direction, then the classical energy per site is given by

$$\varepsilon_{\text{cl}}^{120°} = -(\Gamma - \Gamma')\cos(\varphi_A + \varphi_B - \pi). \quad (4)$$

The optimal angles of φ_A and φ_B depend on the sign of $\Gamma - \Gamma'$, where a negative sign denotes $\varphi_A + \varphi_B = 0$ or 2π [see Fig. 1(c)], while a positive sign represents $\varphi_A + \varphi_B = \pi$ or 3π [see Fig. 1(d)]. There is no extra restriction on the values of φ_A and φ_B, implying an emergent $U(1)$ symmetry in the ab plane. In both cases, we have the classical energy as $\varepsilon_{\text{cl}}^{120°} = -|\Gamma - \Gamma'|$.

In addition, we also parametrize $\Gamma = \cos\psi$ and $\Gamma' = \sin\psi$, and show the classical phase diagram in Fig. 1(e). It can be found that the AFM$_c$ phase is preferred when $\psi \in (0, \psi_0)$ with $\psi_0 = \pi - \tan^{-1}(2) \approx 0.6476\pi$ and occupies nearly one third of the whole ψ circle. Remarkably, when $\psi = \pi/4$ (i.e., $\Gamma = \Gamma'$), the Γ-Γ' model can be reduced to

$$\mathcal{H} = \Gamma \sum_{\langle ij \rangle} \left[-\frac{1}{2}(\tilde{S}_i^+ \tilde{S}_j^- + \tilde{S}_i^- \tilde{S}_j^+) + 2\tilde{S}_i^z \tilde{S}_j^z \right], \quad (5)$$

which is nothing but an easy-axis XXZ model with a $\mathbb{Z}_2 \ltimes U(1)$ symmetry. The AFM$_c$ phase and the FM$_c$ phase are smoothly connected to the hidden $SU(2)$ Heisenberg model at $(J, \Gamma, \Gamma') = (1/3, 1/3, 1/3)$ and $(J, \Gamma, \Gamma') = (1/3, -2/3, -2/3)$ [62], respectively. Besides, from the pinnacles of the energy curve shown in Fig. 1(f) we can tell that all the classical phase transitions are of first order. In what follows, we take $\Gamma = 1$ as the energy unit.

B. Linear spin-wave theory

Classically, there is a direct $120°$-AFM$_c$ transition in the vicinity of the AFM Γ limit as Γ' is varied. The quantum fluctuation manifests its effect by altering the underlying phases at least in two aspects [45]. One is that the $120°$ phase is replaced by the zigzag phase when Γ' is negative. The other is that, for small but positive Γ' interaction, there are two exotic phases, which are intervened between the magnetically ordered states. Here we show that the LSWT is amenable to illuminate the effect of quantum fluctuation. Within the framework of LSWT, the quadratic Hamiltonian in the momentum space reads [57]

$$\overline{\mathcal{H}} = NS(S+1)\varepsilon_{\text{cl}} + \frac{S}{2}\sum_q \hat{\mathbf{x}}_q^\dagger \hat{\mathbf{H}}_q \hat{\mathbf{x}}_q, \quad (6)$$

where $\hat{\mathbf{x}}_q^\dagger = (a_{1,q}^\dagger, a_{2,q}^\dagger, \cdots, a_{1,-q}, b_{2,-q}, \cdots)$ is the Nambu spinor and $\hat{\mathbf{H}}_q$ is a 2×2 block matrix termed Bogliubov-de Gennes (BdG) Hamiltonian. The length of Nambu spinor should be $2n_s$ where n_s is the number of sites in one unit cell. The bosonic BdG Hamiltonian is diagonalized via a para-unitary matrix $\mathbf{T}_q$,

$$\mathbf{T}_q^\dagger \hat{\mathbf{H}}_q \mathbf{T}_q = \begin{pmatrix} \boldsymbol{\Omega}_q & 0 \\ 0 & \boldsymbol{\Omega}_{-q} \end{pmatrix}, \quad (7)$$
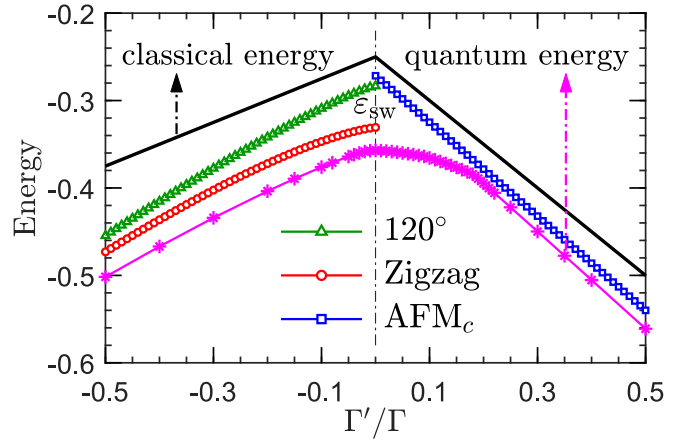
FIG. 2. The spin-wave energy ε_{sw} for the zigzag phase (red circle), $120°$ phase (green triangle), and AFM$_c$ phase (blue square) in the Γ-Γ' model. The classical (black line) and quantum (pink diamond) energy per site with $S = 1/2$ are also shown for comparison.

where $\boldsymbol{\Omega}_q = \text{diag}(\omega_{q1}, \omega_{q2}, \cdots, \omega_{qn_s})$ whose diagonal elements are the magnon dispersions ω_{qv} ($v = 1, 2, \cdots, n_s$). The para-unitary matrix $\mathbf{T}_q$ satisfies the boson relation

$$\mathbf{T}_q^\dagger \boldsymbol{\Sigma} \mathbf{T}_q = \mathbf{T}_q \boldsymbol{\Sigma} \mathbf{T}_q^\dagger = \boldsymbol{\Sigma}, \quad (8)$$

where $\boldsymbol{\Sigma} = \text{diag}(+\hat{\mathbf{1}}, -\hat{\mathbf{1}})$. In other words, the magnon dispersions ω_{qv} can also be determined by diagonalizing $\boldsymbol{\Sigma}\hat{\mathbf{H}}_q$. The spin-wave energy is then given by

$$\varepsilon_{\text{sw}} = S(S+1)\varepsilon_{\text{cl}} + \frac{S}{2n_s} \sum_{\{v\} \in n_s} \int \frac{d^2\mathbf{q}}{(2\pi)^2} \omega_{qv}. \quad (9)$$

Figure 2 shows the spin-wave energy ε_{sw} for the zigzag phase, $120°$ phase, and AFM$_c$ phase in the window of $-0.5 \leqslant \Gamma'/\Gamma \leqslant 0.5$. When $\Gamma' < 0$, energy of the zigzag phase is considerably smaller than that of the $120°$ phase, showing that the quantum fluctuation would provoke the zigzag ordering as the true ground state. In the neighboring of the AFM Γ limit, magnon gap Δ of the zigzag phase decreases gradually and vanishes when $\Gamma'/\Gamma = 0$ (not shown). This phenomenon is called the magnon instability and is a signature of phase transition [64]. Hence, the zigzag phase can not surpass the line of $\Gamma'/\Gamma = 0$ and thus cannot survive in the presence of an AFM Γ' term. Whereas the AFM$_c$ phase is favored for modest positive Γ' interaction, there is a noteworthy energy jump between the zigzag phase and the AFM$_c$ phase near $\Gamma'/\Gamma = 0$. Our spin-wave result implies that an intermediate region should exist as a consequence of competing interactions. The classical (black line) and quantum (pink diamond) energy per site are also shown in Fig. 2 for comparison. It is observed that the spin-wave energy is lower than the classical energy, but is higher than the quantum case.

IV. MAGNETIC FIELD-INDUCED QUANTUM PHASE DIAGRAM

In a previous study of the Γ-Γ' model by the authors [45], it is shown that there is indeed an intermediate region between the zigzag phase and the AFM$_c$ phase at the quantum level. In
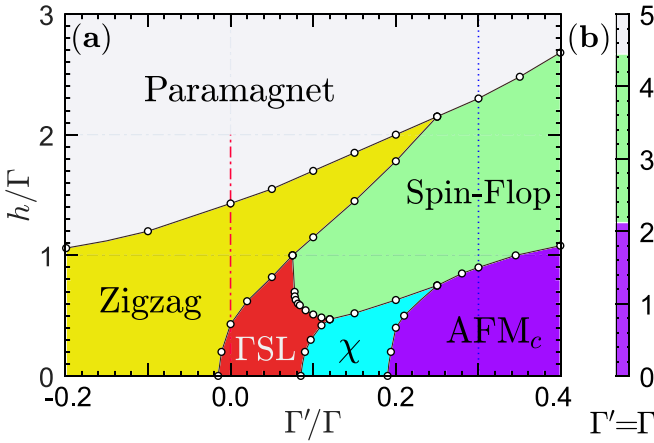
FIG. 3. (a) Quantum phase diagram of the Γ-Γ' model in a [111] magnetic field. The DMRG calculation is performed on a 24-site hexagonal cluster. The phase diagram contains a zigzag phase, a ΓSL, a chiral spin state (marked by the symbol χ), and an AFM$_c$ phase at zero field. A spin-flop phase and a paramagnetic phase are induced upon increasing the magnetic field. We note that the precise phase boundary between the zigzag phase and the paramagnetic phase is smeared due to the unavoidable multistep magnetization before entering into the totally polarized region. The vertical cuts along the lines of $\Gamma'/\Gamma = 0.0$ (red dash-dotted line) and $\Gamma'/\Gamma = 0.3$ (blue dotted line) are the main focuses of the following study. The study of other cuts are shown in the Supplemental Material [61]. (b) Quantum phase transitions along the line of $\Gamma'/\Gamma = 1$. The low-field transition at $h_{t1} = 2.115(3)$ is first order, while the high-field transition at $h_{t2} \approx 4.50$ seems to be continuous.

the range of $-0.015 \lesssim \Gamma'/\Gamma \lesssim 0.095$, there is a gapless ΓSL, which is characterized by a hidden plaquette correlation [42]. Besides, a chiral-spin ordered state with spontaneously time-reversal symmetry breaking appears when $0.095 \lesssim \Gamma'/\Gamma \lesssim 0.185$. Here, we go beyond that study by applying an out-of-plane magnetic field, and the resulting phase diagram is shown in Fig. 3. The DMRG computation is mainly executed in the 24-site hexagonal cluster. We have also checked the phase diagram on the YC6 cylinder of 12×6, which basically remains unchanged despite a tiny shift of the phase boundaries.

Throughout the phase diagram, there are six distinct phases and two of them only exist in the presence of a finite magnetic field. One is a conventional paramagnetic phase, while the other is a spin-flop phase, which also exhibits an in-plane magnetization when compared with the paramagnetic phase. Starting from the magnetically ordered states at zero field, transition between the zigzag phase and the paramagnetic phase is first order, as reflected by the jump in the magnetic order parameter. By contrast, the spin-flop phase is sandwiched between the AFM$_c$ phase and the paramagnetic phase. We note that the spin-flop phase has an intimate relation to the superfluid phase identified in the extended Bose-Hubbard model [49,50]. In addition, the regions of ΓSL and chiral spin state are enlarged but are terminated before entering into the paramagnetic phase. In what follows we will concentrate on the ΓSL and chiral spin state, while leaving the discussion on the spin-flop phase to the next section.
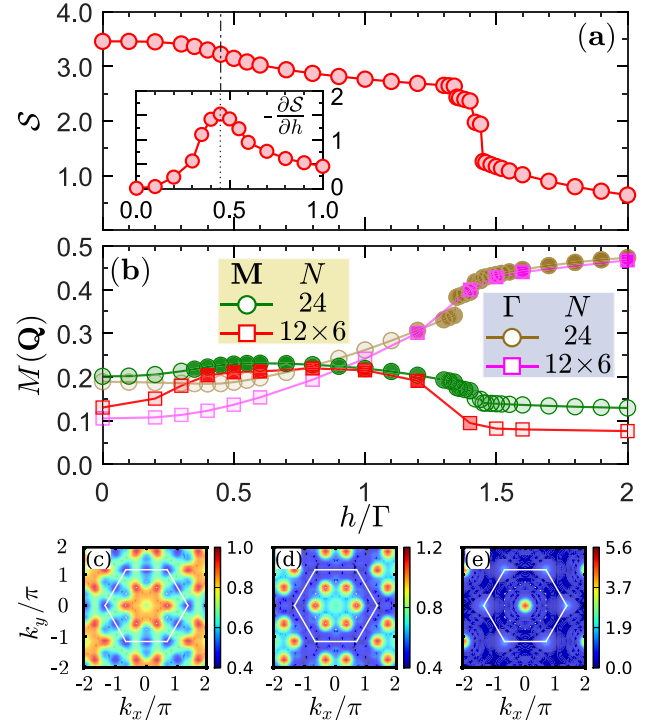

FIG. 4. (a) Behavior of the entanglement entropy $\mathcal{S}$ as a function of magnetic field h in the Γ-Γ' model with $\Gamma'/\Gamma = 0$. The underlying geometry is a 24-site hexagonal cluster. Inset: The first-order derivative of $\mathcal{S}$ with respect to h. (b) Magnetic order parameters $M_N(\mathbf{Q})$ for the zigzag order and paramagnetic phase with $\mathbf{Q} = \mathbf{M}$ and $\mathbf{\Gamma}$, respectively. The geometries are a 24-site hexagonal cluster and a 12×6 YC cylinder. (c)–(e) show the static structure factor at a field of (c) $h = 0.2$ (ΓSL), (d) $h = 1.0$ (zigzag phase), and (e) $h = 2.0$ (paramagnetic phase), respectively.

A. ΓSL in the magnetic field

We start from the ΓSL and investigate its fate in the presence of a magnetic field. The von Neumann entanglement entropy is a reliable quantity to capture the phase transitions between the phases with unique ground states. It is defined as $\mathcal{S} = -\mathrm{tr}(\rho_s \ln \rho_s)$ where ρ_s is the reduced density matrix of one-half of the system [65]. $\mathcal{S}$ displays a jump at the transition point if the transition is first order, otherwise it varies smoothly with the driving parameter. Figure 4(a) shows the behavior of entanglement entropy $\mathcal{S}$ on the 24-site cluster. When we apply a small magnetic field, entanglement entropy is maintained around 3.5, followed by a sustaining decrease with a steepest drop at $h_{t1} \approx 0.45(5)$ (see inset). The entanglement entropy does not experience a big change until an abrupt reduction around $h_{t2} \approx 1.40(5)$. The consecutive release of entropy therein may imply a multistep alignment of the spins towards a more parallel structure in the paramagnetic phase. We expect the interval of this metastate shrinks with the increase of the system size.

To figure out the nature of the intermediate region, we resort to the static structure factor (SSF) $\mathbb{S}_{N,\tau}(\mathbf{q}) = \sum_{\alpha\beta} \delta_{\alpha\beta} \mathbb{S}_{N,\tau}^{\alpha\beta}(\mathbf{q})$ where

$$\mathbb{S}_{N,\tau}^{\alpha\beta} = \frac{1}{N} \sum_{ij} \left(\langle S_i^\alpha S_j^\beta \rangle - \tau \langle S_i^\alpha \rangle \langle S_j^\beta \rangle \right) e^{i\mathbf{q} \cdot (\mathbf{R}_i - \mathbf{R}_j)}. \quad (10)$$

Here, $\boldsymbol{R}_i$ is the position of site i and $\boldsymbol{q}$ is the wave vector in the reciprocal space. The symbol τ could be either 0 or 1, and it indicates that the effect of magnetic field is either kept or deducted, respectively. We note that when $\tau = 1$, only the intensity around the very center (i.e., $\boldsymbol{\Gamma}$ point) in the Brillouin zone is reduced. Figures 4(c), 4(d) and 4(e), show the snapshots of SSF $\mathbb{S}_{N,\tau}(\mathbf{Q})$ in a field of $h = 0.1$ ($\tau = 1$), 1.0 ($\tau = 1$), and 2.0 ($\tau = 0$), respectively. In Fig. 4(c), intensity in the reciprocal space is very diffusive, albeit with a soft peak at $\mathbf{M}$ point that may relate to the adjacent zigzag ordering. By contrast, a sharp peak at $\mathbf{M}$ point could be spotted in the intermediate region as shown in Fig. 4(d). Upon applying a higher magnetic field, there is a paramagnetic phase, which displays a visible peak at $\boldsymbol{\Gamma}$ point [see Fig. 4(e)]. We define the order parameter $M_{N,\tau}(\mathbf{Q}) = \sqrt{\mathbb{S}_{N,\tau=0}(\mathbf{Q})/N}$ with $\mathbf{Q}$ being the ordering wave vector. In Fig. 4(b) we show the order parameters $M_N(\mathbf{Q})$ of the zigzag phase ($\mathbf{Q} = \mathbf{M}$) and paramagnetic phase ($\mathbf{Q} = \boldsymbol{\Gamma}$) on a 24-site hexagonal cluster and a 12×6 YC cylinder. When $h < h_{t,1}$, the order parameter $M_N(\mathbf{M})$ exhibits a considerable reduction with the increase of the system size. Although we do not make an extrapolation of this order parameter for the lack of large clusters, the magnetic order is likely to vanish as N increases, and the low-field region should be identical to the ΓSL identified in the zero-field study [42]. On the other hand, the ground state at $h > h_{t,2}$ is a paramagnetic phase with an almost saturated magnetic moment. However, the most inspiring observation is that there is a zigzag ordering, which is smoothly connected to the zigzag phase induced by the FM Γ' interaction, in the intermediate region of $h_{t,1} < h < h_{t,2}$. The zigzag phase is unusual in that it only has a unique ground state with a small excitation gap.

Similar to the Kitaev honeycomb model, in the Γ-Γ' model we also calculate the hexagonal plaquette operator [3]

$$\hat{W}_p = 2^6 S_1^x S_2^y S_3^z S_4^x S_5^y S_6^z, \tag{11}$$

where the sites 1–6 form a hexagon plaquette labeled by p [see Fig. 1(a)]. Without loss of generality, we define the fluxlike density $\overline{W}_p = \sum_p \langle \hat{W}_p \rangle / N_p$ where $N_p = N/2$ is the number of plaquette. Figure 5(a) shows the fluxlike density $\overline{W}_p$ with respect to the magnetic field. In the ΓSL region the net flux $\overline{W}_p$ is $-0.25(2)$ at zero field, followed by a steady ascent as the field increases. The fluxlike density finally becomes positive and reach its maximal value of $0.10(1)$ at $h_{t,2}$. After that one enters into the paramagnetic phase accompanied by a sudden drop of $\overline{W}_p$. It is interesting to note that the fluxlike density in the paramagnetic phase does not has a monotonous behavior; instead, it first declines with the field and then increases again, reaching a saturated value ultimately. For large enough magnetic field along the [111] direction, all the spins $\mathbf{S}_i = \boldsymbol{\sigma}_i/2$ are totally polarized with the same magnitude, $\langle \sigma_i^x \rangle = \langle \sigma_i^y \rangle = \langle \sigma_i^z \rangle = 1/\sqrt{3}$. Thus, the expectation value of hexagonal plaquette operator at large enough magnetic field is

$$\langle \hat{W}_p \rangle = \left(\frac{1}{\sqrt{3}} \right)^6 = \frac{1}{27} \approx 0.037037\cdots. \tag{12}$$

As can be seen from the inset of Fig. 5(a), $\overline{W}_p$ indeed approaches to $1/27$ with the increase of magnetic field.
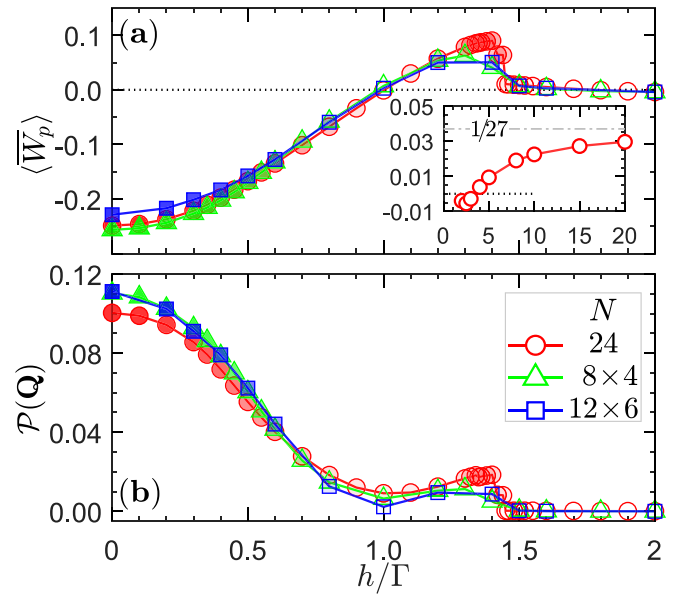

FIG. 5. (a) Fluxlike density $\langle \overline{W}_p \rangle$ and (b) plaquette order parameter $\mathcal{P}(\mathbf{Q})$ on the 24-site hexagonal cluster (red circle) and the YC cylinders of 8×4 (green triangle) and 12×6 (blue square). The inset of (a) shows $\langle \overline{W}_p \rangle$ at large field, which tends to approach $1/27$ as field increases.

We continue the discussion of hexagonal plaquette operator by calculating the plaquette-plaquette correlation $\langle W_p \cdot W_q \rangle$. The plaquette structure factor is defined as [66]

$$\mathcal{W}_{N_p}(\boldsymbol{q}) = \frac{1}{N_p} \sum_{pq} \langle \hat{W}_p \hat{W}_q \rangle e^{i\boldsymbol{q}\cdot(\boldsymbol{R}_p - \boldsymbol{R}_q)}, \tag{13}$$

where $\boldsymbol{R}_p$ is the central position of each plaquette, which forms a triangular lattice with a lattice constant of $\sqrt{3}$. In the totally polarized phase, $\langle \hat{W}_p \cdot \hat{W}_q \rangle$ can only take three different values, depending on their relative positions. If $\hat{W}_p$ and $\hat{W}_q$ are identical or totally irrelevant without any shared edge, then $\langle \hat{W}_p \cdot \hat{W}_q \rangle$ is 1 and $1/3^6$, respectively. Otherwise, $\hat{W}_p$ and $\hat{W}_q$ have a sole shared edge and $\langle \hat{W}_p \cdot \hat{W}_q \rangle = 1/3^5$. Taken together, we have

$$\mathcal{W}_{N_p}(\boldsymbol{\Gamma}) = \left(1 + \frac{11}{3^6} \right) + \frac{N_p}{3^6}. \tag{14}$$

Typically, the first term in the right-hand side is dominant when $N \lesssim 100$. To reduce the strong finite-size effect, we introduce the following plaquette order parameter:

$$\mathcal{P}_{N_p} = \sqrt{\frac{\mathcal{W}_{N_p}(\mathbf{Q})}{N_p}} - \frac{1}{\sqrt{N_p}}. \tag{15}$$

Figure 5(b) shows the plaquette order parameter $\mathcal{P}(\mathbf{Q})$ with the high-symmetry point $\mathbf{Q} = \boldsymbol{\Gamma}$ being the center of the Brillouin zone. In the ΓSL and the zigzag phase, $\mathcal{P}(\boldsymbol{\Gamma})$ is nonzero as the spins are noncollinear. Furthermore, $\mathcal{P}(\boldsymbol{\Gamma})$ is more pronounced in the ΓSL, highlighting the unusual spin pattern due to the intrinsic frustration.
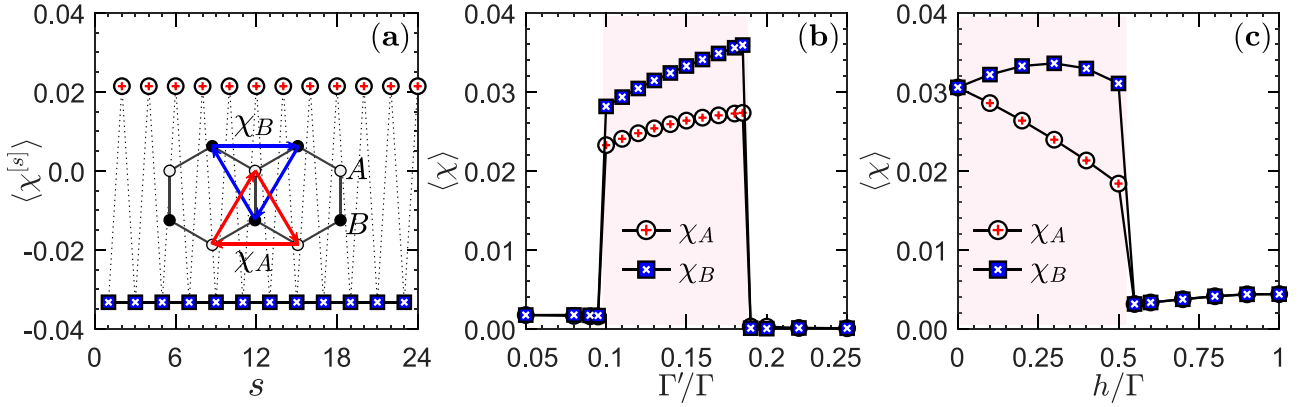
FIG. 6. (a) Chiral distribution of $\langle \chi_{ijk}^{[s]} \rangle$ as a function of site index s on a 24-site hexagonal cluster with $\Gamma'/\Gamma = 0.15$ and $h = 0.2$. Here, s is the center site of the equilateral triangle formed by (i, j, k). When s is 2, 4, 6,... (red circle), (i, j, k) should be odd and belongs to the A sublattice with the chiral order parameter $\langle \chi_A \rangle = |\langle \chi^{[s]} \rangle|$ (s is even). Otherwise, when s is 1, 3, 5,... (blue square), (i, j, k) belongs to the B sublattice with the chiral order parameter $\langle \chi_B \rangle = |\langle \chi^{[s]} \rangle|$ (s is odd). (b) Behaviors of $\langle \chi_A \rangle$ (red circle) and $\langle \chi_B \rangle$ (blue square) as functions of Γ'/Γ with fixed $h = 0.2$. (c) Behaviors of $\langle \chi_A \rangle$ (red circle) and $\langle \chi_B \rangle$ (blue square) as functions of h with fixed $\Gamma'/\Gamma = 0.15$.

B. Chiral spin state

As pointed out in Ref. [45], the chiral-spin ordered state could be stabilized by a small AFM Γ' interaction that is one order of magnitude smaller than the dominated Γ interaction. It is known to break time-reversal symmetry spontaneously and thus exhibits a finite scalar spin chirality defined as

$$\hat{\chi}_{ijk}^{\triangle} = \hat{\mathbf{S}}_i \cdot (\hat{\mathbf{S}}_j \times \hat{\mathbf{S}}_k), \quad (16)$$

where (i, j, k) label lattice sites of either A or B sublattice, forming an equilateral triangle $\triangle$ in the clockwise direction, see inset of Fig. 6(a). We find that the chiral spin state could still survive up to a small magnetic field, before entering into a partially polarized phase. Following the analysis in Ref. [45], we focus on a point at $(\Gamma' = 0.15, h = 0.2)$ in the Γ-Γ' model, and the distribution of chirality $\hat{\chi}$ within the 24-site cluster is shown in Fig. 6(a). It is clearly seen that the scalar spin chirality is uniformly distributed in each sublattice and possesses an opposing sign in the A and B sublattices. In addition, magnitudes of the chirality in the A and B sublattices, whose absolute values are $\langle \chi_A \rangle \approx 0.0264$ and $\langle \chi_B \rangle \approx 0.0333$, are no longer the same due to the existence of the magnetic field.

Figure 6(b) presents the chiral order parameters $\langle \chi_A \rangle$ and $\langle \chi_B \rangle$ as functions of Γ'. The chiral order parameters are very robust in the window of $0.095 \lesssim \Gamma'/\Gamma \lesssim 0.185$ and undergo drastic jumps on the brink of phase boundaries. We also show the evolutions of chiral order parameters with respect to the magnetic field in Fig. 6(c). It is found that $\langle \chi_B \rangle$ is slightly elevated with the increase of magnetic field and displays a maximum when $h \approx 0.3$. By contrast, $\langle \chi_A \rangle$ decreases almost linearly from 0.0333 (at $h = 0.0$) to 0.0195 (at $h_t \approx 0.53$). Again, the chiral order parameters experience jumps to a small but finite value at $h > h_t$, and the system enters into the spin-flop phase where the discrepancy between $\langle \chi_A \rangle$ and $\langle \chi_B \rangle$ disappears.

According to our previous work, the chiral spin state is known as a magnetically disordered state without long-range magnetic ordering [45]. In that study, we proposed that it could be either a gapless chiral spin liquid because of the

continuous feature of the dynamic structure factor in the low frequency region, or a symmetry-protected phase with short-range entanglement based on the modular matrix. However, a decisive conclusion could hardly be made due to the low symmetry of the Hamiltonian and the capacity of the numerical calculation. Hence, determining the nature of the chiral spin state is a tempting open question to be explored.

V. FIELD-INDUCED SPIN-FLOP PHASE

A. Overview of the classical analysis

In this section, we investigate the evolution of the AFM$_c$ phase under the [111] magnetic field in the region of $\Gamma, \Gamma' > 0$. Since the applied magnetic field is parallel to the direction of the classical magnetic moment, the energy of the AFM$_c$ phase remains unchanged in the presence of a weak magnetic field. By contrast, a strong enough field will induce a totally polarized phase where all the spins align along the magnetic field direction. To quantify the value of the critical field h_t, we define the spin $\mathbf{S}_i$ for arbitrary i as

$$\mathbf{S}_i = S(\sin \vartheta \cos \varphi \hat{\mathbf{a}} + \sin \vartheta \sin \varphi \hat{\mathbf{b}} + \cos \vartheta \hat{\mathbf{c}}), \quad (17)$$

where $\hat{\mathbf{a}}[11\bar{2}]$, $\hat{\mathbf{b}}[\bar{1}10]$, and $\hat{\mathbf{c}}[111]$ are the crystallographic axes, ϑ and φ are the polar angle relative to the c axis and azimuthal angle in the ab plane, respectively. We note that this ansatz is certainly suitable for the paramagnetic phase, but may break down for the unpolarized phases and thus should be checked by other methods in the intermediate region. By using of Eq. (17), the entire variational classical energy $e_g = E_g/NS^2$ is given by

$$e_g = \frac{\Gamma + 2\Gamma'}{4}(1 + 3\cos 2\vartheta) - \frac{h}{S}\cos \vartheta. \quad (18)$$

Strikingly, the energy is irrelevant of φ and thus the polar angle ϑ is the sole variational parameter [67]. The optimal value ϑ_o is determined by the conditional equations $\partial e_g/\partial \vartheta = 0$ and $\partial e_g^2/\partial \vartheta^2 > 0$, and from which we obtain that

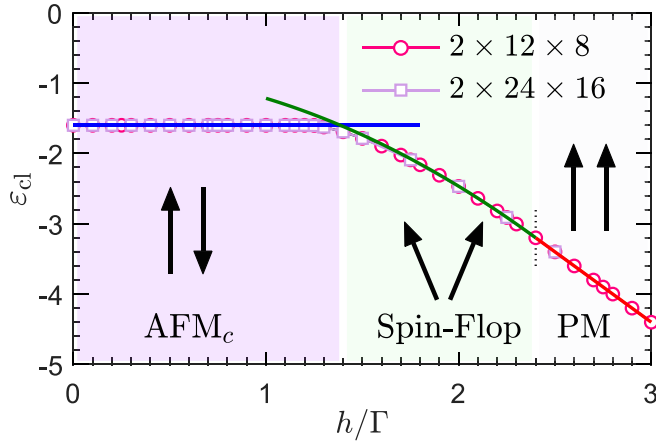$$\vartheta_o = \begin{cases} 0, & h \geqslant h_t \\ \cos^{-1}(h/h_t), & h < h_t \end{cases}, \quad (19)$$

FIG. 7. Classical MC calculation of the ground-state energy $\varepsilon_{\rm cl}$ as a function of magnetic field h/Γ ($S = 1/2$) in the Γ-Γ' model with $\Gamma'/\Gamma = 0.3$. Two distinct clusters, $2 \times 12 \times 8$ (open circle) and $2 \times 24 \times 16$ (open square), are used in the simulation. The exact energy of the AFM$_c$ phase (blue line, left), spin-flop phase (green line, middle), and paramagnetic phase (red line, right) are shown for comparison. The cartoon patterns of these phases are shown in the inset.

where $h_t = 3S(\Gamma + 2\Gamma')$ is the critical magnetic field. Equation (19) indicates that just below the critical magnetic field h_t, the spins deviate from the axial direction by a given angle ϑ_o and exhibit a nonzero in-plane magnetization (see the inset of Fig. 7). With the decrease of the magnetic field, the energy of the intermediate phase grows, and it is replaced by the AFM$_c$ phase when $h < h_t/\sqrt{3}$. By substituting Eq. (19) into Eq. (18) and with the energy of the AFM$_c$ phase in mind, we have the classical energy of the three phases

$$
e_g = \begin{cases} -\frac{3h - h_t}{3S}, & h \geqslant h_t \\ -\frac{3h^2 + h_t^2}{6Sh_t}, & h_t/\sqrt{3} < h < h_t \\ -\frac{h_t}{3S}, & h \leqslant h_t/\sqrt{3} \end{cases} \tag{20}
$$

One could notice that all the three phases have two-site unit cells, see the cartoon patterns shown in Fig. 7.

Having discussed the consecutive transitions along the magnetic field, we now perform the parallel tempering MC simulation to study the intermediate region in detail. After identifications of the possible classical ground states, we then perform the simulation on two cylinders of $2 \times 12 \times 8$ (open circle) and $2 \times 24 \times 16$ (open square). The calculated energy of the AFM$_c$ phase (blue line) and the paramagnetic phase (red line) match nicely with the exact solutions shown in Eq. (20), see Fig. 7. In the intermediate region, there are several large-unit-cell orderings and the selected configurations are shown in the Supplemental Material [61]. These results are at odds with Eq. (17), which assumes that all the spins have the same polar angle. We note that, while the spin-flop phase (green line) is not the genuine ground state in the intermediate region, its energy is very close to and yet slightly higher than the MC result. This leaves the possibility open to legitimate the spin-flop phase at the quantum level.

B. Spin-wave dispersions, topological magnons, and order-by-disorder mechanism

In this section, we resort to the LSWT to study the magnon excitations of the underlying phases in the [111] magnetic field. We start from the AFM$_c$ phase at the low-field region and its BdG Hamiltonian in Eq. (6) takes the form of

$$
\hat{\hat{H}} = \begin{pmatrix} \varepsilon_0^+ & \lambda_0(\boldsymbol{q}) & 0 & \lambda_1(\boldsymbol{q}) \\ \lambda_0^*(\boldsymbol{q}) & \varepsilon_0^- & \lambda_1(-\boldsymbol{q}) & 0 \\ 0 & \lambda_1^*(-\boldsymbol{q}) & \varepsilon_0^+ & \lambda_0^*(-\boldsymbol{q}) \\ \lambda_1^*(\boldsymbol{q}) & 0 & \lambda_0(-\boldsymbol{q}) & \varepsilon_0^- \end{pmatrix}. \tag{21}
$$

The momentum-dependent coupling expressions are

$$
\varepsilon_0^\pm = 2(\Gamma + 2\Gamma') \pm h/S, \tag{22}
$$

$$
\lambda_0(\boldsymbol{q}) = 2(\Gamma - \Gamma')\gamma_{1,\boldsymbol{q}}, \tag{23}
$$

$$
\lambda_1(\boldsymbol{q}) = -(\Gamma + 2\Gamma')\gamma_{0,\boldsymbol{q}}. \tag{24}
$$

For convenience, we introduce three auxiliary functions

$$
\gamma_{0,\boldsymbol{q}} = \tfrac{1}{3}(e^{\iota \boldsymbol{q}\delta_x} + e^{\iota \boldsymbol{q}\delta_y} + e^{\iota \boldsymbol{q}\delta_z}), \tag{25}
$$

$$
\gamma_{1,\boldsymbol{q}} = \tfrac{1}{3}(\omega^{-1} e^{\iota \boldsymbol{q}\delta_x} + \omega e^{\iota \boldsymbol{q}\delta_y} + e^{\iota \boldsymbol{q}\delta_z}), \tag{26}
$$

$$
\gamma_{2,\boldsymbol{q}} = \tfrac{1}{3}(\omega e^{\iota \boldsymbol{q}\delta_x} + \omega^{-1} e^{\iota \boldsymbol{q}\delta_y} + e^{\iota \boldsymbol{q}\delta_z}), \tag{27}
$$

which satisfy the relations $\gamma_{0,\boldsymbol{q}}^* = \gamma_{0,-\boldsymbol{q}}$, $\gamma_{1,\boldsymbol{q}}^* = \gamma_{2,-\boldsymbol{q}}$, and $\gamma_{2,\boldsymbol{q}}^* = \gamma_{1,-\boldsymbol{q}}$. The Berry curvature $\mathcal{F}_\upsilon(\boldsymbol{q})$ associated with each magnon band is given by

$$
\mathcal{F}_\upsilon(\boldsymbol{q}) = \frac{\partial \mathcal{A}_y^{(\upsilon)}(\boldsymbol{q})}{\partial q_x} - \frac{\partial \mathcal{A}_x^{(\upsilon)}(\boldsymbol{q})}{\partial q_y}, \tag{28}
$$

where $\mathcal{A}_\gamma^{(\upsilon)}(\boldsymbol{q}) = \iota \text{Tr}[\mathcal{P}_\upsilon \boldsymbol{\Sigma} \boldsymbol{T}_{\boldsymbol{q}}^\dagger \boldsymbol{\Sigma}(\partial_{q_\gamma} \boldsymbol{T}_{\boldsymbol{q}})]$ ($\gamma = x, y$) is the Berry potential. Here, $\mathcal{P}_\upsilon$ is a diagonal matrix taking $+1$ for the υth diagonal component and zero otherwise. Alternatively, the Berry curvature can be rewritten as [68]

$$
\mathcal{F}_\upsilon(\boldsymbol{q}) = -2\text{Im}\left[\sum_{\mu \neq \upsilon} \sigma_{\mu\upsilon} \frac{\langle \boldsymbol{T}_\upsilon | \partial_{q_x}\hat{\hat{H}} | \boldsymbol{T}_\mu \rangle \langle \boldsymbol{T}_\mu | \partial_{q_y}\hat{\hat{H}} | \boldsymbol{T}_\upsilon \rangle}{(\omega_{\boldsymbol{q}\mu} - \omega_{\boldsymbol{q}\upsilon})^2} \right] \tag{29}
$$

with $\sigma_{\mu\upsilon} = \Sigma_{\mu\mu}\Sigma_{\upsilon\upsilon}$. The Chern number of the υth branch is obtained as the sum of the Berry curvature in the Brillouin zone,

$$
\mathcal{C}_\upsilon = \frac{1}{2\pi} \int_{\rm BZ} \mathcal{F}_\upsilon(\boldsymbol{q}) d^2\boldsymbol{q}. \tag{30}
$$

Figure 8(a) shows two magnon branches along the high-symmetry points in the Brillouin zone in the zero-field limit, and the intensity of the lower branch in the reciprocal space is shown in Fig. 8(b). The **K** and **K**$'$ points are inequivalent, which is reminiscent of the time-reversal symmetry breaking. The magnon bands are gapped and the lowest excitation gap comes from the **K** point with the value of

$$
\Delta_{\mathbf{K}} = 2(\Gamma + 2\Gamma') - \sqrt{(h/S)^2 + 4(\Gamma - \Gamma')^2}. \tag{31}
$$

Apparently, the zero-field magnon gap $\Delta_{\mathbf{K}} = 6\Gamma' = 1.8$, consistent with the data shown in Fig. 8(a). However, one finds that depending on the relative magnitude of the magnetic field
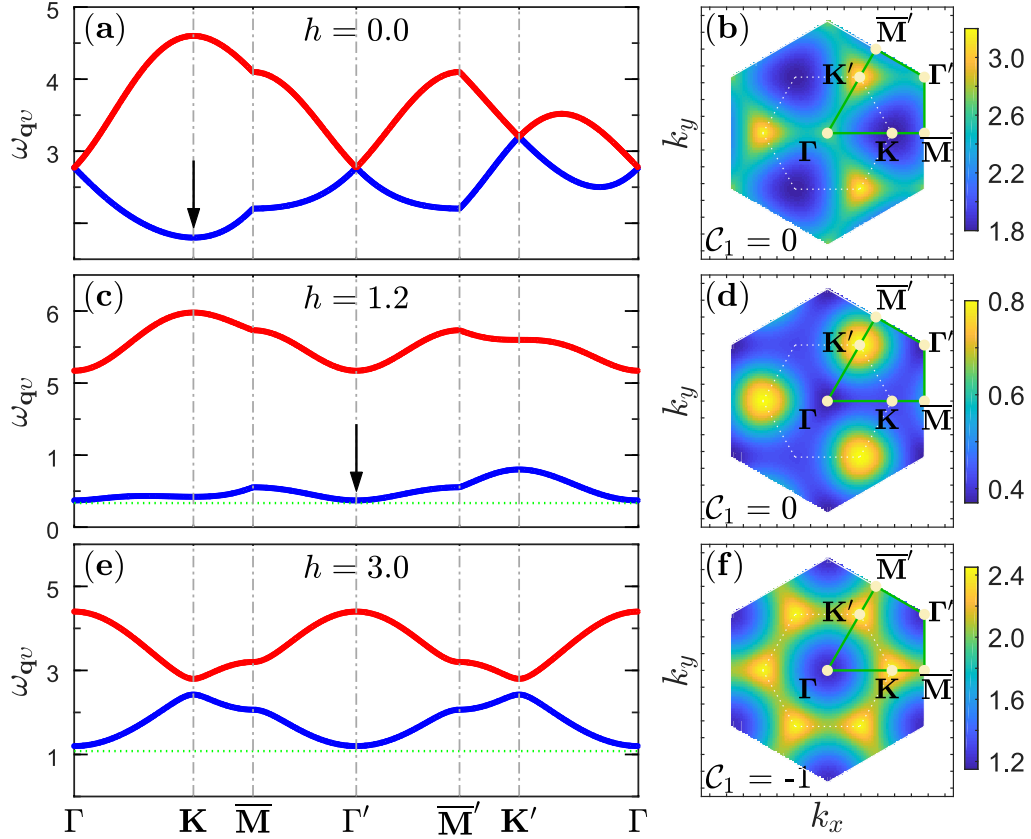
FIG. 8. Magnon dispersions ω_{q1} (blue) and ω_{q2} (red) of the AFM$_c$ phase or the paramagnetic phase in the $S = 1/2$ Γ-Γ' model with $\Gamma'/\Gamma = 0.3$. (a) and (b) show the magnon dispersions and the intensity of the lowest magnon branch in the AFM$_c$ phase with $h = 0.0$, respectively. The black arrow in (a) marks the position of the minimal excitation gap, and the path in the reciprocal space is depicted in (b). (c), and (d) show the same quantities as these of (a) and (b) in the case of AFM$_c$ phase with $h = 1.2$. The green dotted horizontal line in (c) is a guide for the eye. (e) and (f) show the same quantities as these of (a) and (b) in the case of paramagnetic phase with $h = 3.0$. The green dotted horizontal line in (e) is a guide for the eye. In this paramagnetic phase, the Chern number $\mathcal{C}_1$ of the lowest magnon branch is -1.

there could be a soft mode around the ordering wave vectors of Γ/Γ' points. Hence, the lowest excitation gap is given by

$$\Delta_{\Gamma'} = \sqrt{3}(\Gamma + 2\Gamma') - h/S, \quad (32)$$

which decreases linearly with the increase of magnetic field. In Fig. 8(c), we show the magnon dispersions at a field of $h = 1.2$, together with a lower magnon branch in Fig. 8(d). It is observed that excitation gap at Γ' point is slightly smaller than that of the $\mathbf{K}$ point. Since the melting of the AFM$_c$ ordering is accompanied by the closure of excitation gap at Γ' point, the lower transition point is estimated as $h_{t1} = \sqrt{3}S(\Gamma + 2\Gamma')$.

We also calculate the Chern numbers and find that they are zero for both branches. The reason may be that the two branches touch each other at some points and thus the Chern number is not well defined. We note that the same conclusion was drawn in a relevant study [69]. However, it is demonstrated that magnons in the paramagnetic phase is topologically nontrivial for the existence of nonzero Chern number [70–72]. To this end, we proceed with the analysis of the paramagnetic phase at large enough magnetic field.

Similarly, the BdG Hamiltonian of the paramagnetic phase takes the form of

$$\varepsilon_0^{\pm} = -2(\Gamma + 2\Gamma') + h/S, \quad (33)$$

$$\lambda_0(\mathbf{q}) = -(\Gamma + 2\Gamma')\gamma_{0,\mathbf{q}}, \quad (34)$$

$$\lambda_1(\mathbf{q}) = 2(\Gamma - \Gamma')\gamma_{1,\mathbf{q}}. \quad (35)$$

The magnon spectrum at the $\mathbf{\Gamma}$ point is

$$\Delta_{\mathbf{\Gamma}} = h/S - 3(\Gamma + 2\Gamma'), \quad (36)$$

which increases linearly with the magnetic field when h is larger than the upper transition point $h_{t2} = 3S(\Gamma + 2\Gamma')$. Figure 8(e) shows the dispersion of the paramagnetic phase where $h = 3.0$ is taken as an example. It can be verified that the magnon gap at $\mathbf{\Gamma}$ is 1.2, which is in accordance with the theoretical value revealed in Eq. (36). More importantly, our result suggests that the Chern numbers of the two branches in the paramagnetic phase are -1 and $+1$, respectively, see Fig. 8(f).

The LSWT analysis shows clearly that there should be an intermediate region in the window of $h \in (h_{t1}, h_{t2})$, which happens to be the same interval inferred from the classical study [see Eq. (20)]. For the spin-flop phase, the classical
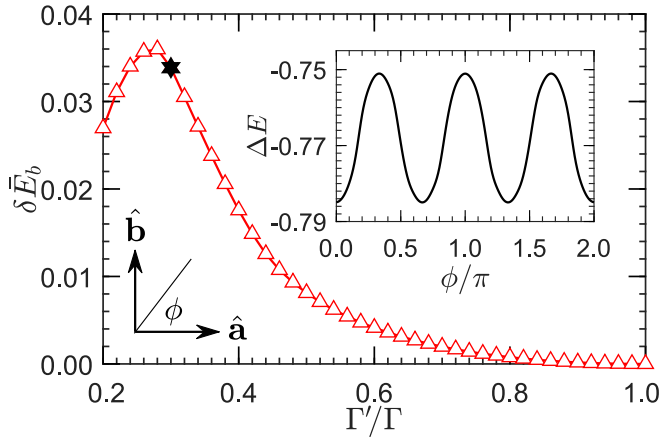
FIG. 9. Energy barrier $\delta\bar{E}_b$ between the spin-flop phase of different orientations along the line of $h = 9(\Gamma + 2\Gamma')/8$. Inset: Spin-wave energy correction $\Delta E(\varphi)$ at the parameter point $(\Gamma'/\Gamma, h) = (0.3, 1.8)$ vs azimuthal angle φ, which is suited at the $\hat{\mathbf{a}}$-$\hat{\mathbf{b}}$ plane.

moment direction $\mathbf{S}_i(\vartheta, \varphi)$ is shown in Eq. (17) where ϑ is given by Eq. (19). According to Eq. (9) we calculate the spin-wave energy $\varepsilon_{\mathrm{sw}}$ at a magnetic field of $h = 1.8$, and the energy reduction $\Delta E(\varphi) = \varepsilon_{\mathrm{sw}} - S^2\varepsilon_{\mathrm{cl}}$ with respect to the azimuthal angle φ is shown in the inset of Fig. 9. It is shown that $\Delta E(\varphi)$ exhibits a period of $2\pi/3$ in the in-plane manifold and the angles at $\varphi = 0$, $2\pi/3$, and $4\pi/3$ are more energetically favorable than the others. Hence, the emergent classical $U(1)$ manifold is lifted by quantum fluctuations, generating a discrete C_3 rotational symmetry. We also introduce the energy barrier $\delta\bar{E}_b$ as $E_g(\varphi = \pi) - E_g(\varphi = 0)$, which is 0.0338 when $(\Gamma'/\Gamma, h) = (0.3, 1.8)$ (marked by a hexagram in Fig. 9). In the main panel of Fig. 9, we present the energy barrier $\delta\bar{E}_b$ along the line of $h = 9(\Gamma + 2\Gamma')/8$. The value of $\delta\bar{E}_b$ gradually raises with the increase of Γ'/Γ up to $\Gamma'/\Gamma \approx 0.27$. Afterwards, it drops rapidly and vanishes at $\Gamma'/\Gamma = 1$ where the system possesses a hidden $U(1)$ symmetry.

C. DMRG calculation

In Sec. V B, we predict that a spin-flop phase can occur in a wide field region before entering into the paramagnetic phase. Here, we confirm the existence of such phase by the DMRG method. Figure 10(a) shows the first 15 low-lying excitation gaps $\Delta_v = E_v - E_0$ in the Γ-Γ' model with $\Gamma'/\Gamma = 0.3$ fixed. The method to target the first few low-lying energy levels simultaneously is shown in Ref. [42]. With the increase of the magnetic field, the excitation gap Δ_2 of the AFM$_c$ phase goes down gradually and is vanishingly small at $h_{t1} = 0.88(2)$. Beyond the transition point, excitation gaps are small and the spectrum is very dense in a large interval, indicative of a gapless region. Exceeding $h_{t2} = 2.38(2)$, excitation gap Δ_1 opens linearly with the magnetic field. We note in passing that the transition points are fairly consistent with those obtained by cylinder DMRG calculation [61]. In addition, magnetic order parameters of the AFM$_c$ phase and the paramagnetic phase are shown in Fig. 10(b). For the AFM$_c$ phase, the SSF peaks at the $\boldsymbol{\Gamma}'$ point, and the order parameter $M(\boldsymbol{\Gamma}')$ has a sharp jump at h_{t1}, signifying a first-order transition thereof. In the intermediate phase, the spins are only partially polarized as
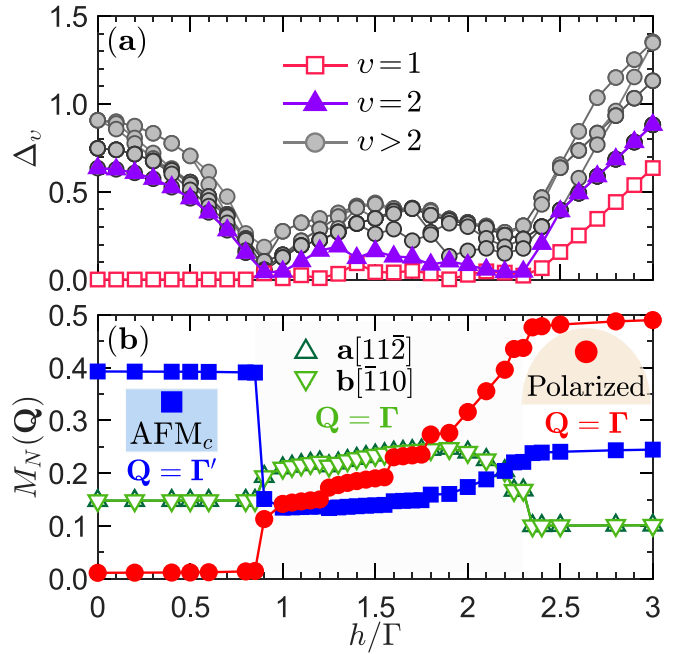

FIG. 10. (a) The first 15 excitation gaps Δ_v ($v = 1 - 15$) as functions of magnetic field h/Γ in the Γ-Γ' model with $\Gamma'/\Gamma = 0.3$. (b) Magnetic order parameters $M_N(\mathbf{Q})$ for the AFM$_c$ phase and paramagnetic phase with $\mathbf{Q} = \boldsymbol{\Gamma}'$ (blue square) and $\boldsymbol{\Gamma}$ (red circle), respectively. The intermediate spin-flop phase has a finite in-plane magnetization (green triangles).

opposed to the paramagnetic phase when $h_t > h_{t2}$. However, a nontrivial observation is that it also has a uniform in-plane correlation that is perpendicular to the external field. For example, magnetization along $\hat{\mathbf{a}}$ and $\hat{\mathbf{b}}$ are of equal strength and are overlapped in the plot [see Fig. 10(c)]. Consequently, the intermediate phase is recognized as a gapless spin-flop phase with a temporarily emergent $U(1)$ symmetry. The finite-size scaling of the order parameters and the SSF of the spin-flop phase are shown in the Supplemental Material [61].

However, the in-plane component of the spin-flop phase is likely unstable against extra perturbation. The emergent $U(1)$ symmetry is then broken down to C_3 rotational symmetry, accompanied by the appearance of gapless Goldstone modes. To this end, we apply a tilted magnetic field $\mathbf{h} = h(\vartheta, \varphi)$, which enjoys the same form of Eq. (17). Here, the intensity of the field $h = 1.8$ and the tilted angle ϑ relative to the c axis is specified as $2°$, $5°$, and $8°$. Figure 11 shows the behaviors of the shifted ground-state energy ΔE_g, which is defined as $E_g - \bar{E}_g$ with $\bar{E}_g = \frac{1}{2\pi}\int_0^{2\pi} d\varphi E_g(\varphi)$, with respect to the in-plane azimuthal angle $\varphi \in [0, 2\pi)$ [73]. It can be observed that the variation of the energy is one order of magnitude smaller than that of the semiclassical situation. However, in both cases there is a breaking of the continuous $U(1)$ symmetry to the discrete C_3 rotational symmetry, giving rise to three local minima when $\varphi = 0$, $2\pi/3$, and $4\pi/3$. In addition, the energy barrier $\delta\bar{E}_b = \Delta E_g(\varphi = \pi) - \Delta E_g(\varphi = 0)$ obeys approximately the fitting formula $\delta\bar{E}_b \approx 10^{-3} \cdot \frac{7.1\vartheta}{9.6+\vartheta}$, showing that the energy barrier $\delta\bar{E}_b$ will be less sensitive to the tilted angle ϑ as ϑ increases. To conclude, there is a two-step symmetry changing in the spin-flop phase. The first step is
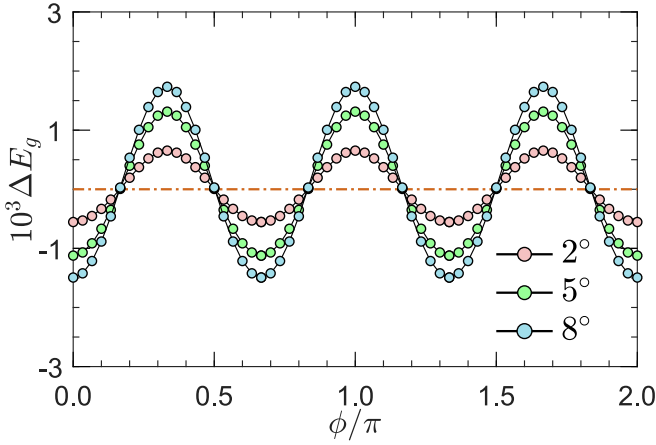
FIG. 11. Behaviors of the shifted ground-state energy ΔE_g in the range of $\varphi \in [0, 2\pi)$ for three different tilted angle $\vartheta = 2°$ (pink), $5°$ (green), and $8°$ (blue) in the Γ-Γ' model under a c-axis magnetic field. Here, the DMRG calculation is performed on a 24-site cluster with $(\Gamma'/\Gamma, h) = (0.3, 1.8)$. The energy valleys at $\varphi = 0$, $2\pi/3$, and $4\pi/3$ are reminiscent of the order-by-disorder phenomenon.

from the discrete symmetry to the emergent $U(1)$ symmetry, while the second step is from $U(1)$ symmetry to the broken C_3 rotational symmetry. We note that a similar phenomenon is also reported in the classical honeycomb Γ model in a magnetic field [48].

As shown in Fig. 3(b), the spin-flop phase could survive for at least $\Gamma'/\Gamma = 1$, at which the model is equivalent to the spin-1/2 XXZ model in a longitudinal magnetic field with an easy-axis anisotropy $\Delta_a = 2$. Accidentally, the spin-flop phase could also be interpreted as the superfluid phase in the extended Bose-Hubbard model whose Hamiltonian reads [49,50]

$$\mathcal{H}_{\mathrm{BH}} = -t \sum_{\langle ij \rangle} (b_i^\dagger b_j + b_i b_j^\dagger) + V \sum_{\langle ij \rangle} n_i n_j - \mu \sum_i n_i$$
$$+ \frac{U}{2} \sum_i n_i (n_i - 1), \qquad (37)$$

where $b_i^\dagger$ (b_i) is the creation (annihilation) operator at site i and $n_i = b_i^\dagger b_i$ is the corresponding occupation number. Here, t is the nearest-neighbor hopping parameter, μ is the chemical potential, and U and V represent the on-site and nearest-neighbor repulsive interactions, respectively. In the hard-core limit where $U/t \to \infty$, there is one boson at most on each site. By virtue of the mapping $b_i^\dagger = S_i^+$, $b_i = S_i^-$, and $n_i = S_i^z + 1/2$, Eq. (37) can be mapped onto the spin-1/2 XXZ model under a longitudinal magnetic field,

$$\overline{\mathcal{H}} = 2t \Big[\sum_{\langle ij \rangle} \big[-(S_i^x S_j^x + S_i^y S_j^y) + \Delta_a S_i^z S_j^z \big] - h \sum_i S_i^z \Big] + E_0,$$
$$(38)$$

where $\Delta_a = V/2t$ is the anisotropy of the spin-spin interaction, $h = \frac{1}{2t}(\mu - zV/2) = \Delta(\mu/V - z/2)$ is the longitudinal magnetic field, and $E_0 = -\frac{NV}{2}(\mu/V - z/4)$ is an energy constant arising from the mapping between the spins and bosons operators. Considering the case $t/V = 1/4$ (inversely, we

have $\Delta_a = V/2t = 2$) and $\mu/V > z/2 = 1.5$ in the original extended Bose-Hubbard model, the ground state is a solid with density $\rho = 1/2$ when μ/V is slightly increased, a $\rho = 1$ Mott insulator at large enough μ/V, and a superfluid at moderate μ/V. In view of the relation $\mu_t/V = (h_t + z)/2$ with $h_{t,1} = 2.115(3)$ and $h_{t,2} = 4.5$, our result suggests the first transitions occurs at $\mu_{t,1}/V = 2.558(2)$ and $\mu_{t,2}/V = 3.75$, which is fairly consistent with quantum Monte Carlo simulations (for illustration, see Refs. [49,50] and also Supplemental Material [61]).

VI. CONCLUSION

In this paper we focus on the interplay of magnetic field and trigonal distortion [18] in honeycomb Γ model. For this purpose, we have studied a Γ-Γ' model in a [111] magnetic field in the vicinity of a dominated AFM Γ region. In the absence of magnetic field, a $120°$ phase and an AFM$_c$ phase can be selected immediately from the infinitely degenerate ground state of the classical Γ model, depending on the sign of Γ' interaction. The classical $120°$ phase is unstable against quantum fluctuations, giving away to the neighboring zigzag ordering. At the quantum level, two exotic phases are found to exist in the intermediate region between the zigzag phase and the AFM$_c$ phase. One is a ΓSL stemming from the ground state of honeycomb Γ model, while the other is a chiral spin state, which spontaneously breaks the time-reversal symmetry. Upon applying a magnetic field, regions of the ΓSL and chiral spin state are enlarged but are terminated before entering the paramagnetic phase at large field.

A nontrivial observation of this work is that there is a field-induced spin-flop phase as long as a modest magnetic field is applied over the AFM$_c$ phase. The spins in the spin-flop phase are tilted away from the field direction and are free to rotate in the honeycomb plane, indicative of an emergent $U(1)$ symmetry. Due to the quantum fluctuation in the frustrated magnet, such a continuous symmetry is broken down to the C_3 rotational symmetry where the spins are perpendicular to any of the three types of bonds. When $\Gamma'/\Gamma = 1$, the model is reduced to an easy-axis spin-1/2 XXZ antiferromagnet subjected to a longitudinal magnetic field. In this circumstance, it is equivalent to a hard-core extended Bose-Hubbard model. In that sense, the spin-flop phase is merely the superfluid phase. In doing so, we manifest an unusual route from the Γ region to the XXZ magnet.

In closing, we comment that there are several ways to achieve such a dominated Γ interaction in experiments. In α-RuCl$_3$, for example, the spin interactions are revealed to be sensitive to the layer stacking and octahedral distortion, and the overwhelming Γ regime with a desired AFM Γ' interaction could be achieved upon applying compression [74]. On the other hand, by virtue of the circularly polarized light, the Heisenberg interaction in α-RuCl$_3$ can be made much smaller than the anisotropic exchange interactions K and Γ [75], and the tailored light pulse can further weaken the Kitaev interaction by a proper adjustment of its amplitude and frequency [76,77]. Therefore, these procedures allow us to drive the material into a regime where the Γ interaction is prominent [78].

[1] J. G. Rau, E. K.-H. Lee, and H.-Y. Kee, Spin-orbit physics giving rise to novel phases in correlated systems: Iridates and related materials, Annu. Rev. Condens. Matter Phys. **7**, 195 (2016).

[2] H. Takagi, T. Takayama, G. Jackeli, G. Khaliullin, S. E. Nagler, Concept and realization of Kitaev quantum spin liquids, Nature Rev. Phys. **1**, 264 (2019).

[3] A. Kitaev, Anyons in an exactly solved model and beyond, Ann. Phys. (NY) **321**, 2 (2006).

[4] G. Jackeli and G. Khaliullin, Mott Insulators in the Strong Spin-Orbit Coupling Limit: From Heisenberg to a Quantum Compass and Kitaev Models, Phys. Rev. Lett. **102**, 017205 (2009).

[5] X. Liu, T. Berlijn, W.-G. Yin, W. Ku, A. Tsvelik, Young-June Kim, H. Gretarsson, Yogesh Singh, P. Gegenwart, and J. P. Hill, Long-range magnetic ordering in Na_2IrO_3, Phys. Rev. B **83**, 220403(R) (2011).

[6] J. Chaloupka, G. Jackeli, and G. Khaliullin, Zigzag Magnetic Order in the Iridium Oxide Na_2IrO_3, Phys. Rev. Lett. **110**, 097204 (2013).

[7] K. W. Plumb, J. P. Clancy, L. J. Sandilands, V. V. Shankar, Y. F. Hu, K. S. Burch, H.-Y. Kee, and Y.-J. Kim, α-$RuCl_3$: a Spin-Orbit Assisted Mott Insulator on a Honeycomb Lattice, Phys. Rev. B **90**, 041112(R) (2014).

[8] H.-S. Kim, V. V. Shankar, A. Catuneanu, and H.-Y. Kee, Kitaev magnetism in honeycomb $RuCl_3$ with intermediate spin-orbit coupling, Phys. Rev. B **91**, 241110(R) (2015).

[9] R. D. Johnson, S. C. Williams, A. A. Haghighirad, J. Singleton, V. Zapf, P. Manuel, I. I. Mazin, Y. Li, H. O. Jeschke, R. Valentí, and R. Coldea, Monoclinic crystal structure of α-$RuCl_3$ and the zigzag antiferromagnetic ground state, Phys. Rev. B **92**, 235119 (2015).

[10] A. Biffin, R. D. Johnson, I. Kimchi, R. Morris, A. Bombardi, J. G. Analytis, A. Vishwanath, and R. Coldea, Noncoplanar and Counterrotating Incommensurate Magnetic Order Stabilized by Kitaev Interactions in γ-Li_2IrO_3, Phys. Rev. Lett. **113**, 197201 (2014).

[11] S. C. Williams, R. D. Johnson, F. Freund, S. Choi, A. Jesche, I. Kimchi, S. Manni, A. Bombardi, P. Manuel, P. Gegenwart, and R. Coldea, Incommensurate counterrotating magnetic order stabilized by Kitaev interactions in the layered honeycomb α-Li_2IrO_3, Phys. Rev. B **93**, 195158 (2016).

[12] I. Rousochatzakis and N. B. Perkins, Magnetic field induced evolution of intertwined orders in the Kitaev magnet β-Li_2IrO_3, Phys. Rev. B **97**, 174423 (2018).

[13] J. Xing, E. Feng, Y. Liu, E. Emmanouilidou, C. Hu, J. Liu, D. Graf, A. P. Ramirez, G. Chen, H. Cao, and N. Ni, Néel-type antiferromagnetic order and magnetic field-temperature phase diagram in the spin-$\frac{1}{2}$ rare-earth honeycomb compound $YbCl_3$, Phys. Rev. B **102**, 014427 (2020).

[14] G. Sala, M. B. Stone, B. K. Rai, A. F. May, D. S. Parker, G. B. Halász, Y. Q. Cheng, G. Ehlers, V. O. Garlea, Q. Zhang, M. D. Lumsden, and A. D. Christianson, Crystal field splitting, local anisotropy, and low-energy excitations in the quantum magnet $YbCl_3$, Phys. Rev. B **100**, 180406(R) (2019).

[15] Y. Hao, H. Wo, Y. Gu, X. Zhang, Y. Gu, S. Zheng, Y. Zhao, G. Xu, J. W. Lynn, K. Nakajima, N. Murai, W. Wang, and J. Zhao, Field-tuned magnetic structure and phase diagram of the honeycomb magnet $YbCl_3$, Sci. China Phys. Mech. Astron. **64**, 237411 (2021).

[16] G. Sala, M. B. Stone, B. K. Rai, A. F. May, P. Laurell, V. O. Garlea, N. P. Butch, M. D. Lumsden, G. Ehlers, G. Pokharel, A. Podlesnyak, D. Mandrus, D. S. Parker, S. Okamoto, G. B. Halász, and A. D. Christianson, Van Hove singularity in the magnon spectrum of the antiferromagnetic quantum honeycomb lattice, Nature Commun. **12**, 171 (2021).

[17] J. G. Rau, E. K.-H. Lee, and H.-Y. Kee, Generic Spin Model for the Honeycomb Iridates beyond the Kitaev Limit, Phys. Rev. Lett. **112**, 077204 (2014).

[18] J. G. Rau and H.-Y. Kee, Trigonal distortion in the honeycomb iridates: Proximity of zigzag and spiral phases in Na_2IrO_3, arXiv:1408.4811.

[19] A. Banerjee, C. A. Bridges, J.-Q. Yan, A. A. Aczel, L. Li, M. B. Stone, G. E. Granroth, M. D. Lumsden, Y. Yiu, J. Knolle, S. Bhattacharjee, D. L. Kovrizhin, R. Moessner, D. A. Tennant, D. G. Mandrus, and S. E. Nagler, Proximate Kitaev quantum spin liquid behaviour in a honeycomb magnet, Nature Mater. **15**, 733 (2016).

[20] A. Banerjee, J. Yan, J. Knolle, C. A. Bridges, M. B. Stone, M. D. Lumsden, D. G. Mandrus, D. A. Tennant, R. Moessner, and S. E. Nagler, Neutron scattering in the proximate quantum spin liquid α-$RuCl_3$, Science **356**, 1055 (2017).

[21] K. Ran, J. Wang, W. Wang, Z.-Y. Dong, X. Ren, S. Bao, S. Li, Z. Ma, Y. Gan, Y. Zhang, J. T. Park, G. Deng, S. Danilkin, S.-L. Yu, J.-X. Li, and J. Wen, Spin-Wave Excitations Evidencing the Kitaev Interaction in Single Crystalline α-$RuCl_3$, Phys. Rev. Lett. **118**, 107203 (2017).

[22] I. A. Leahy, C. A. Pocs, P. E. Siegfried, D. Graf, S.-H. Do, K.-Y. Choi, B. Normand, and M. Lee, Anomalous Thermal Conductivity and Magnetic Torque Response in the Honeycomb Magnet α-$RuCl_3$, Phys. Rev. Lett. **118**, 187203 (2017).

[23] J. A. Sears, Y. Zhao, Z. Xu, J. W. Lynn, and Y.-J. Kim, Phase Diagram of α-$RuCl_3$ in an in-plane Magnetic Field, Phys. Rev. B **95**, 180411(R) (2017).

[24] S.-H. Baek, S.-H. Do, K.-Y. Choi, Y. S. Kwon, A. U. B. Wolter, S. Nishimoto, J. van den Brink, and B. Büchner, Evidence for a Field-Induced Quantum Spin Liquid in α-RuCl$_3$, Phys. Rev. Lett. **119**, 037201 (2017).

[25] A. U. B. Wolter, L. T. Corredor, L. Janssen, K. Nenkov, S. Schönecker, S.-H. Do, K.-Y. Choi, R. Albrecht, J. Hunger, T. Doert, M. Vojta, and B. Büchner, Field-induced quantum criticality in the Kitaev system α-RuCl$_3$, Phys. Rev. B **96**, 041405(R) (2017).

[26] Z. Wang, S. Reschke, D. Hüvonen, S.-H. Do, K.-Y. Choi, M. Gensch, U. Nagel, T. Room, and A. Loidl, Magnetic Excitations and Continuum of a Possibly Field-Induced Quantum Spin Liquid in α-RuCl$_3$, Phys. Rev. Lett. **119**, 227202 (2017).

[27] J. Zheng, K. Ran, T. Li, J. Wang, P. Wang, B. Liu, Z.-X. Liu, B. Normand, J. Wen, and W. Yu, Gapless Spin Excitations in the Field-Induced Quantum Spin Liquid Phase of α-RuCl$_3$, Phys. Rev. Lett. **119**, 227208 (2017).

[28] S. M. Winter, K. Riedl, P. A. Maksimov, A. L. Chernyshev, A. Honecker, and R. Valenti, Breakdown of magnons in a strongly spin-orbital coupled magnet, Nature Commun. **8**, 1152 (2018).

[29] D. Wulferding, Y. Choi, S.-H. Do, C. H. Lee, P. Lemmens, C. Faugeras, Y. Gallais, and K.-Y. Choi, Magnon bound states versus anyonic Majorana excitations in the Kitaev honeycomb magnet α-RuCl$_3$, Nature Commun. **11**, 1603 (2020).

[30] Y. Kasahara, T. Ohnishi, N. Kurita, H. Tanaka, J. Nasu, Y. Motome, T. Shibauchi, and Y. Matsuda, Majorana quantization and half-integer thermal quantum Hall effect in a Kitaev spin liquid, Nature (London) **559**, 227 (2018).

[31] W. Wang, Z.-Y. Dong, S.-L. Yu, and J.-X. Li, Theoretical investigation of magnetic dynamics in α-RuCl$_3$, Phys. Rev. B **96**, 115103 (2017).

[32] J. A. Sears, L. E. Chern, S. Kim, P. J. Bereciartua, S. Francoual, Y. B. Kim, and Y.-J. Kim, Ferromagnetic Kitaev interaction and the origin of large magnetic anisotropy in α-RuCl$_3$, Nature Phys. **16**, 837-840 (2020).

[33] J. A. Sears, M. Songvilay, K. W. Plumb, J. P. Clancy, Y. Qiu, Y. Zhao, D. Parshall, and Y.-J. Kim, Magnetic order in α-RuCl$_3$: A honeycomb-lattice quantum magnet with strong spin-orbit coupling, Phys. Rev. B **91**, 144420 (2015).

[34] P. A. Maksimov and A. L. Chernyshev, Rethinking α-RuCl$_3$, Phys. Rev. Research **2**, 033011 (2020).

[35] E. C. Andrade, L. Janssen, and M. Vojta, Susceptibility anisotropy and its disorder evolution in models for Kitaev materials, Phys. Rev. B **102**, 115160 (2020).

[36] D. Takikawa and S. Fujimoto, Impact of off-diagonal exchange interactions on the Kitaev spin-liquid state of α-RuCl$_3$, Phys. Rev. B **99**, 224409 (2019).

[37] D. Takikawa and S. Fujimoto, Topological phase transition to Abelian anyon phases due to off-diagonal exchange interaction in the Kitaev spin liquid state, Phys. Rev. B **102**, 174414 (2020).

[38] Y.-F. Jiang, T. P. Devereaux, and H.-C. Jiang, Field-induced quantum spin liquid in the Kitaev-Heisenberg model and its relation to α-RuCl$_3$, Phys. Rev. B **100**, 165123 (2019).

[39] J. S. Gordon, A. Catuneanu, E. S. Sßorensen, and H.-Y. Kee, Theory of the field-revealed Kitaev spin liquid, Nature Commun. **10**, 2470 (2019).

[40] H.-Y. Lee, R. Kaneko, L. E. Chern, T. Okubo, Y. Yamaji, N. Kawashima, and Y. B. Kim, Magnetic-field induced quantum phases in tensor network dtudy of Kitaev magnets, Nature Commun. **11**, 1639 (2020).

[41] B. H. Kim, S. Sota, T. Shirakawa, S. Yunoki, and Y.-W. Son, Proximate Kitaev system for an intermediate magnetic phase in in-plane magnetic fields, Phys. Rev. B **102**, 140402(R) (2020).

[42] Q. Luo, J. Zhao, H.-Y. Kee, and X. Wang, Gapless quantum spin liquid in a honeycomb Γ magnet, npj Quantum Mater. **6**, 57 (2021).

[43] A. Catuneanu, Y. Yamaji, G. Wachtel, Y.-B. Kim, and H.-Y. Kee, Path to stable quantum spin liquids in spin-orbit coupled correlated materials, npj Quantum Mater. **3**, 23 (2018).

[44] M. Gohlke, G. Wachtel, Y. Yamaji, F. Pollmann, and Y. B. Kim, Quantum spin liquid signatures in Kitaev-like frustrated magnets, Phys. Rev. B **97**, 075126 (2018).

[45] Q. Luo, P. P. Stavropoulos, J. S. Gordon, and H.-Y. Kee, Spontaneous chiral-spin ordering in spin-orbit coupled honeycomb magnets, Phys. Rev. Research **4**, 013062 (2022).

[46] F. B. Anderson and H. B. Callen, Statistical mechanics and field-induced phase transitions of the Heisenberg antiferromagnet, Phys. Rev. **136**, A1068 (1964).

[47] B. R. Morrison, The spin-flop transition in some two-sublattice uniaxial antiferromagnets, Phys. Status Solidi B **59**, 581 (1973).

[48] Z. Tian, Z. Fan, P. Saha, and G.-W. Chern, Honeycomb-lattice Gamma model in a magnetic field: hidden Néel order and spin-flop transition, arXiv:2106.16121.

[49] S. Wessel, Phase diagram of interacting bosons on the honeycomb lattice, Phys. Rev. B **75**, 174301 (2007).

[50] J. Y. Gan, Y. C. Wen, J. Ye, T. Li, S.-J. Yang, and Y. Yu, Extended Bose-Hubbard model on a honeycomb lattice, Phys. Rev. B **75**, 214509 (2007).

[51] L. E. Chern, R. Kaneko, H.-Y. Lee, and Y. B. Kim, Magnetic field induced competing phases in spin-orbital entangled Kitaev magnets, Phys. Rev. Research **2**, 013014 (2020).

[52] S.-S. Zhang, G. B. Halász, and C. D. Batista, Theory of the Kitaev model in a [111] magnetic field, Nature Commun. **13**, 399 (2022).

[53] J. M. Luttinger and L. Tisza, Theory of Dipole Interaction in Crystals, Phys. Rev. **70**, 954 (1946).

[54] D. B. Litvin, The Luttinger-Tisza method, Physica **77**, 205 (1974).

[55] N. Metropolis, A. W. Rosenbluth, M. N. Rosenbluth, A. H. Teller, and E. Teller, Equation of state calculations by fast computing machines, J. Chem. Phys. **21**, 1087 (1953).

[56] K. Hukushima and K. Nemoto, Exchange Monte Carlo method and application to spin glass simulations, J. Phys. Soc. Jpn. **65**, 1604 (1996).

[57] P. A. Maksimov and A. L. Chernyshev, Field-induced dynamical properties of the XXZ model on a honeycomb lattice, Phys. Rev. B **93**, 014418 (2016).

[58] S. R. White, Density matrix formulation for quantum renormalization groups, Phys. Rev. Lett. **69**, 2863 (1992).

[59] I. Peschel, X. Q. Wang, M. Kaulke, and K. Hallberg, *Density-Matrix Renormalization* (Springer, Berlin, 1999).

[60] E. M. Stoudenmire and S. R. White, Studying Two Dimensional Systems With the Density Matrix Renormalization Group, Annu. Rev. Condens. Matter Phys. **3**, 111 (2012).

[61] See Supplemental Material at http://link.aps.org/supplemental/10.1103/PhysRevB.105.174435 for the mapping of the Γ-Γ'

model to the extended Bose-Hubbard model, classical Monte Carlo simulation of the Γ-Γ' model, and DMRG determination of phase transitions, finite-size scaling, and excitation gap in the Γ-Γ' model in [111] magnetic field.

[62] J. Chaloupka and G. Khaliullin, Hidden symmetries of the extended Kitaev-Heisenberg model: Implications for the honeycomb-lattice iridates A_2IrO_3, Phys. Rev. B **92**, 024413 (2015).

[63] I. Rousochatzakis and N. B. Perkins, Classical Spin Liquid Instability Driven By Off-Diagonal Exchange in Strong Spin-Orbit Magnets, Phys. Rev. Lett. **118**, 147204 (2017).

[64] P. A. Maksimov, Z. Zhu, S. R. White, and A. L. Chernyshev, Anisotropic-Exchange Magnets on a Triangular Lattice: Spin Waves, Accidental Degeneracies, and Dual Spin Liquids, Phys. Rev. X **9**, 021017 (2019).

[65] J. Eisert, M. Cramer, and M. B. Plenio, Colloquium: Area laws for the entanglement entropy, Rev. Mod. Phys. **82**, 277 (2010).

[66] P. Saha, Z. Fan, D. Zhang, and G.-W. Chern, Hidden Plaquette Order in a Classical Spin Liquid Stabilized by Strong Off-Diagonal Exchange, Phys. Rev. Lett. **122**, 257204 (2019).

[67] L. Janssen, E. C. Andrade, and M. Vojta, Magnetization processes of zigzag states on the honeycomb lattice: Identifying spin models for α-$RuCl_3$ and Na_2IrO_3, Phys. Rev. B **96**, 064430 (2017).

[68] Y. Lu, X. Guo, V. Koval, and C. Jia, Topological thermal Hall effect driven by spin-chirality fluctuations in frustrated antiferromagnets, Phys. Rev. B **99**, 054409 (2019).

[69] X. Zhu, S. Dong, Y. Lin, R. Mondaini, H. Guo, S. Feng, and R. T. Scalettar, Self-organized bosonic domain walls, Phys. Rev. Research **2**, 013085 (2020).

[70] P. A. McClarty, X.-Y. Dong, M. Gohlke, J. G. Rau, F. Pollmann, R. Moessner, and K. Penc, Topological magnons in Kitaev magnets at high fields, Phys. Rev. B **98**, 060404(R) (2018).

[71] D. G. Joshi, Topological excitations in the ferromagnetic Kitaev-Heisenberg model, Phys. Rev. B **98**, 060405(R) (2018).

[72] Z.-X. Luo and G. Chen, Honeycomb rare-earth magnets with anisotropic exchange interactions, SciPost Phys. Core **3**, 004 (2020).

[73] M. Gohlke, L. E. Chern, H.-Y. Kee, and Y. B. Kim, Emergence of nematic paramagnet via quantum order-by-disorder and pseudo-Goldstone modes in Kitaev magnets, Phys. Rev. Research **2**, 043023 (2020).

[74] P. Peter Stavropoulos *et al.* (unpublished).

[75] N. Arakawa and K. Yonemitsu, Floquet engineering of Mott insulators with strong spin-orbit coupling, Phys. Rev. B **103**, L100408 (2021).

[76] A. Sriram and M. Claassen, Light-induced control of magnetic phases in Kitaev quantum magnets, arXiv:2105.01062.

[77] P. Strobel and M. Daghofer, Comparing the influence of floquet dynamics in various Kitaev-Heisenberg materials, Phys. Rev. B **105**, 085144 (2022).

[78] U. Kumar, S. Banerjee, and S.-Z. Lin, Floquet engineering of Kitaev quantum magnets, arXiv:2111.01316.